

Test of a virtual cylindrical acoustic resonator for determining the Boltzmann constant

This content has been downloaded from IOPscience. Please scroll down to see the full text.

2015 Metrologia 52 S343

(<http://iopscience.iop.org/0026-1394/52/5/S343>)

View [the table of contents for this issue](#), or go to the [journal homepage](#) for more

Download details:

IP Address: 129.6.144.201

This content was downloaded on 20/08/2015 at 17:13

Please note that [terms and conditions apply](#).

Test of a virtual cylindrical acoustic resonator for determining the Boltzmann constant

X J Feng¹, H Lin¹, K A Gillis², M R Moldover² and J T Zhang¹

¹ National Institute of Metrology, Beijing 100013, People's Republic of China

² National Institute of Standards and Technology, Gaithersburg, MD 20899-8360, USA

E-mail: zhangjint@nim.ac.cn

Received 31 March 2015, revised 26 May 2015

Accepted for publication 26 May 2015

Published 19 August 2015



Abstract

We report progress toward determining the Boltzmann constant k_B using the concept of a virtual acoustic resonator, a hypothetical resonator that is mathematically equivalent to a cylindrical cavity with periodic boundary conditions. We derived the virtual resonator by combining the measured frequencies of the longitudinal acoustic modes of two argon-filled, cylindrical cavity resonators in such a way to minimize the effects of the cavities' ends, including transducers and ducts attached to the ends. The cavities had lengths of 80 mm and 160 mm and were operated in their longitudinal $(\ell, 0, 0)$ modes. We explored virtual resonators that combine modes of the two resonators that have nearly the same frequencies. The virtual resonator formed from the $(2, 0, 0)$ mode of the 80 mm resonator combined with the $(4, 0, 0)$ mode of the 160 mm resonator yielded a value for k_B that is, fractionally, only $(0.2 \pm 1.5) \times 10^{-6}$ larger than the 2010 CODATA-recommended value of k_B . (The estimated uncertainty is one standard uncertainty corresponding to a 68% confidence level.) The same virtual resonator yielded values of the pressure derivatives of the speed of sound c in argon, $(\partial c^2/\partial p)_T$ and $(\partial c^2/\partial p^2)_T$, that differed from literature values by 1% and 2%, respectively. By comparison, when each cavity was considered separately, the values of k_B , $(\partial c^2/\partial p)_T$, and $(\partial c^2/\partial p^2)_T$ differed from literature values by up to 7 ppm, 10%, and 5%, respectively. However, combining the results from the $(3, 0, 0)$ or $(4, 0, 0)$ modes of shorter resonator with the results from the $(6, 0, 0)$ or $(8, 0, 0)$ modes of the longer resonator yielded incorrect values of k_B that varied from run-to-run. We speculate that these puzzling results originated in an unmodeled coupling, either between the two cavities (that resonated at nearly identical resonance frequencies in the same pressure vessel) or between the cavities and modes of the pressure vessel.

Keywords: Boltzmann constant, acoustic gas thermometer, acoustic resonator, speed of sound, virtual resonator

(Some figures may appear in colour only in the online journal)

1. Introduction

The Boltzmann constant k_B relates the thermodynamic temperature T to the average energy in a statistical-mechanical degree of freedom. A single molecule of mass m has 3 translational degrees of freedom. When it is in equilibrium with a heat bath, its average kinetic energy is related to the thermodynamic temperature by $(1/2)m v_{\text{RMS}}^2 = (3/2)k_B T$, where v_{RMS}

is the root-mean-square velocity of a molecule. In an ideal gas of such molecules, v_{RMS} is connected to the zero-density speed of sound c_0 and the zero-density heat-capacity ratio $C_p^0/C_v^0 \equiv \gamma_0$ of the gas through $v_{\text{RMS}}^2 = (3/\gamma_0)c_0^2$. For a monatomic gas γ_0 is exactly 5/3. For an ideal gas, k_B is obtained by:

$$k_B = c_0^2 M / (T \gamma_0 N_A) \quad (1)$$

where $M = mN_A$ is the molar mass of gas and N_A is the Avogadro constant, which is known with the relative standard uncertainty of 3×10^{-8} [1].

Since the 1970s, the acoustic determinations of k_B have used values of c_0^2 that were deduced from accurate measurements of the resonance frequencies of cavities of known dimensions that were filled with either helium or argon and maintained at the temperature of the triple point of water, T_{TPW} [2–11]. In principle, c_0^2 could be measured using cavities of any shape [12]. In practice, the lowest uncertainties have been obtained using the radially symmetric modes of spherical or quasi-spherical cavities and the longitudinal modes of cylindrical cavities. Recently, we used single cavities of fixed lengths to measure k_B [10,11]. In connection with these measurements of k_B , we have published a detailed theory of fixed-length cylindrical cavities, as well as our laboratory realizations of such cavities and our experimental procedures [10,11,13–17]. Therefore, it is unnecessary to repeat these details here.

The present work does not report a new estimate of k_B , but explores the advantages and the problems that we encountered when measuring k_B with the virtual cylindrical resonator method. In previous publications [15,18], we described a method by which k_B could be measured more accurately with two cylindrical resonators than with either cylindrical resonator alone. Here, we refine the concept in terms of a *virtual resonator*, that is, a resonator that does not actually exist. A virtual resonator is mathematically equivalent to a cylindrical resonator with periodic boundary conditions instead of end-plates; it is modeled from pairs of longitudinal modes with nominally identical resonance frequencies from two physical cylindrical cavities having different lengths but nominally identical end-plates. The virtual resonator method, discussed in section 2, eliminates hard-to-model effects of end-plates.

The virtual resonator concept has two ancestors. One ancestor is the procedure of the National Physical Laboratory (NPL) for the measurement of k_B during the 1970s that used a cylindrical acoustic resonator with a moveable end (an acoustic interferometer) that was displaced an accurately measured distance. The second ancestor is the remarkably successful method of generating calculable capacitance changes by using cylindrical cross capacitors containing a tubular guard that is displaced an accurately measured distance while maintaining constant end effects [19].

As shown schematically in figure 1, we used two fixed-length cavity resonators that had lengths of 80 mm and 160 mm. The 80 mm resonator was operated in its longitudinal $(\ell, 0, 0)$ modes, and the 160 mm resonator was operated in its $(2\ell, 0, 0)$ modes with $\ell = 2, 3,$ and 4 for both resonators. Here, we identify the modes $(\ell, 0, 0)$ using the notation of Gillis [20]. We simply identify the modes by the index ℓ . The ends of the cavities were designed to be identical. Any differences in the physical or material properties between the fabricated end-plates introducing second-order effects were deemed to be inconsequential. Because both resonators operated at nearly identical resonance frequencies and had nearly identical end-plates, the acoustic admittances of the ends, which are frequency-dependent and hard to calculate, were the same as first-order. By using the theory of virtual

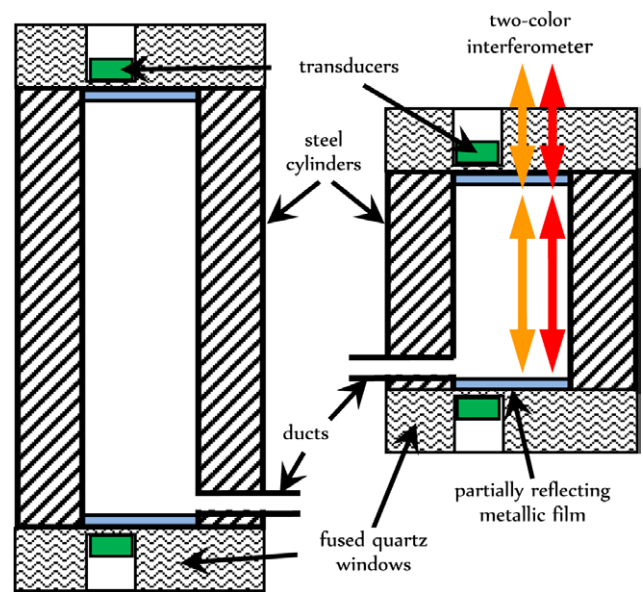


Figure 1. Schematic diagram of two resonators used to make a virtual resonator.

resonators, these admittances cancel out to first-order in our calculation of k_B .

The virtual resonator formed by combining data in the two resonators near 3.8 kHz [the $(2, 0, 0)$ mode of the shorter resonator and the $(4, 0, 0)$ mode of the longer resonator] yielded a value of k_B that was, fractionally, only $(0.2 \pm 1.5) \times 10^{-6}$ larger than the 2010 CODATA-recommended value of k_B , and the pressure derivatives of the speed of sound c in argon, $(\partial c^2/\partial p)_T$ and $(\partial c^2/\partial p^2)_T$, were within 1% and 2%, respectively, of the widely recognized literature values. The virtual resonator from the combined modes near 5.8 kHz [the $(3, 0, 0)$ mode in the shorter resonator and the $(6, 0, 0)$ mode in the longer resonator] and the virtual resonator from the combined modes near 7.7 kHz [the $(4, 0, 0)$ mode in the shorter resonator and the $(8, 0, 0)$ mode in the longer resonator] yielded poor values for k_B that differed by up to 7×10^{-6} from CODATA and varied from run to run *in a way that we do not understand*.

In this article, we review the theory of the virtual resonator, describe key features of the measurements, and discuss the uncertainties that might be expected. We describe the puzzling, run-dependent results and planned changes that, we hope, will solve the puzzle.

2. Theory of the virtual cylindrical resonator

A virtual cylindrical resonator is a mathematical model used to analyze the resonance frequency and half-width data from the longitudinal gas modes of two gas-filled cylindrical cavities with identical resonance frequencies and identical end-plates but with different lengths. The combined measurements from the two modes are equivalent to a single mode in a hypothetical cylindrical cavity without end-plates. Because the virtual resonator has no end-plates, its mode has a higher effective quality factor (Q) and requires smaller corrections than the modes from either of the actual resonators when analyzed independently.

As a simple example, consider a rigid-walled cylindrical cavity (radius a) with one end-plate that is fixed and one that is a moveable piston. A sound source at a fixed frequency f drives acoustic oscillations in the gas. As described previously [2,3], when the piston is moved to change the length of the cavity, the source excites a series of resonances of the longitudinal gas modes $(\ell, 0, 0)$ when the distance L between the end-plates has specific values L_ℓ . The speed of sound c in the gas may be determined from a single mode by a measurement of L_ℓ . The accuracy of the speed of sound measurement using this technique is limited by the accuracy with which the distance between the piston and the fixed end-plate can be measured. A better technique utilizes two adjacent longitudinal modes and requires a measurement of the displacement of the piston, $\Delta L = L_{\ell+1} - L_\ell$, which can be measured more accurately than the cavity's length.

For an inviscid gas in a perfectly cylindrical cavity bounded by a rigid, insulating wall, the expression for the speed of sound using the single-mode technique is $c = 2fL_\ell/\ell$; using the displacement technique, the expression is $c = 2f\Delta L$. For sound speed measurements in real gases using either technique, the measured length or displacement must be corrected to account for the presence of the viscous and thermal boundary layers whose characteristic lengths (δ_v and δ_t , respectively) depend on the pressure and on the acoustic frequency. However, because f is constant, the lengths δ_v and δ_t do not change as L changes. With the single-mode technique, the expression for the speed of sound is, including the boundary layer corrections,

$$c = \frac{2fL_\ell}{\ell} \left[1 + \frac{\delta_v}{2a} + (\gamma - 1) \frac{\delta_t}{2a} + (\gamma - 1) \frac{\delta_t}{L_\ell} + O\left(\frac{\delta_t^2}{a^2}\right) \right] \quad (2)$$

In equation (2), the second and third terms in the rectangular brackets account for the boundary layers at the cylindrical wall, and the fourth term accounts for the thermal boundary layer at the end-plates. In contrast, the expression for the speed of sound measured with the displacement technique is

$$c = 2f\Delta L \left[1 + \frac{\delta_v}{2a} + (\gamma - 1) \frac{\delta_t}{2a} + O\left(\frac{\delta_t^2}{a^2}\right) \right]. \quad (3)$$

Equation (3) is preferable to equation (2) because the term $(\gamma - 1)\delta_t/L$ that accounts for heat conduction at the end-plates is not present. Furthermore, equation (3) contains the displacement ΔL instead of the length L_ℓ in equation (2). Equation (3) describes a mathematical cylindrical cavity with radius a and length ΔL but with periodic boundary conditions at the ends instead of end-plates. We call this end-free cavity a virtual resonator.

We considered testing the virtual resonator concept using a cylindrical 'acoustic interferometer' (described above) similar to the one used at NPL in the 1970s [2,3]. However, we were discouraged by the challenges of building a cylindrical cavity (with a diameter on the order of 8 cm) terminated by a piston that could be displaced several centimeters along the cylinder's axis while maintaining stable orientation with respect to that axis. Furthermore, the gap (or sliding seal) between

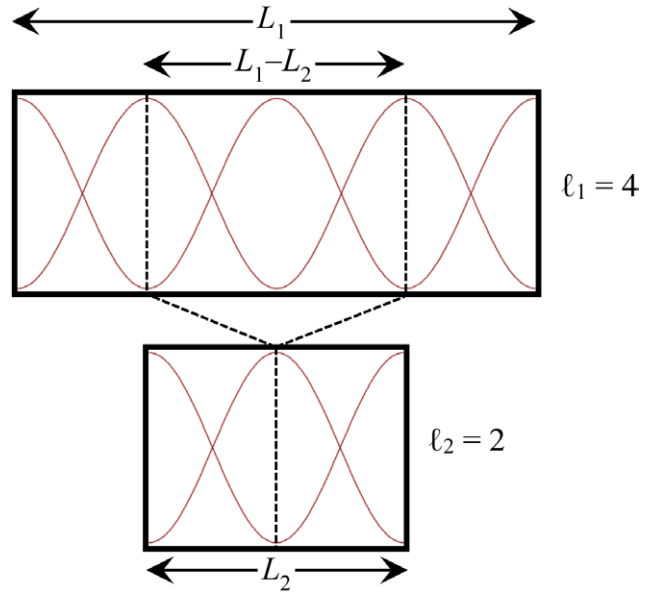


Figure 2. The concept of a virtual resonator derived from measurements in two resonators whose lengths differ by a factor of 2. The longitudinal mode indices differ by a factor of 2, so the frequencies will be nearly equal.

the piston and the cavity's wall must have a stable (preferably predictable), acoustic admittance and it must not contaminate the test gas with impurities at sub-part-per-million levels. To avoid these complexities, we chose to test the virtual-resonator concept by using the two fixed-length (80 mm and 160 mm) resonators as sketched in figure 1.

We designate the longer cavity '1' and the shorter cavity '2.' The sinusoidal curves in figure 2 illustrate the standing pressure waves in the cavities when the modes $\ell_2 = 2$ and $\ell_1 = 4$ are resonant. Because the cavities' lengths and mode indices differ by factors of 2, the wavelength of sound (and therefore the frequency) is the same in both cavities. The dashed lines in figure 2 show how the two halves of resonator-2 are mapped onto the end sections of resonator-1. The center section of resonator-1 inside the dashed lines is the virtual resonator with length $\Delta L_{12} = L_1 - L_2$ and has no end-plates. Thus, from first-order perturbation theory, the surface integral over the acoustic admittance in cavity-1 is the sum of the integral over cavity-2 and the integral over the virtual cavity. A detailed analysis predicts the working equation for the speed of sound in terms of the measured resonance frequencies f_1, f_2 and the measured cavity lengths is (from equation (17) described previously [15])

$$c = \frac{2f_1 f_2 \Delta L_{12}}{\ell_1 f_2 - \ell_2 f_1} \left(1 - \frac{\delta L_{12}}{\Delta L_{12}} \right), \quad (4)$$

where

$$\frac{\delta L_{12}}{\Delta L_{12}} = \frac{L_1}{\Delta L_{12}} \frac{\Delta f_1}{f_1^{(0)}} - \frac{L_2}{\Delta L_{12}} \frac{\Delta f_2}{f_2^{(0)}} \quad (5)$$

is a small correction that depends on the perturbations Δf_1 and Δf_2 for the individual resonators. By design, $\ell_1 = 2\ell_2$, $f_1 \approx f_2$, $L_1/\Delta L_{12} \approx 2$, and $L_2/\Delta L_{12} \approx 1$. Because the frequencies and the

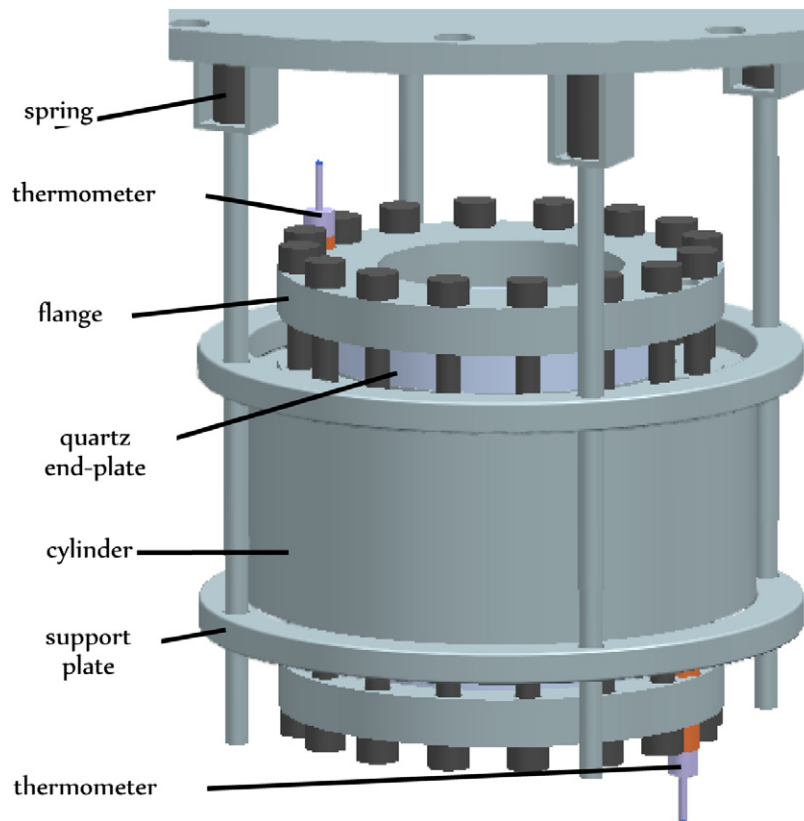


Figure 3. The 80 mm cylindrical resonator and supports.

end-plates in the two resonators are similar, the perturbation from the end-plates caused by the thermal boundary layer cancels out to the first order in equations (4) and (5). Of greater importance, the hard-to-model, frequency-dependent perturbations from the compliance of the end-plates, fill ducts, and transducers built into the end-plates, and from the differences between the optical and acoustic lengths cancel out to the first order in equation (5), provided that the compliances, ducts, transducers, and optical coatings are identical in both end-plates and that the frequencies in both resonators are similar. The analysis of the virtual resonator predicts the resonance half-width is

$$\frac{g_{12}}{f_{12}^{(0)}} = \frac{L_1}{\Delta L_{12}} \frac{g_1}{f_1^{(0)}} - \frac{L_2}{\Delta L_{12}} \frac{g_2}{f_2^{(0)}}, \quad (6)$$

where g_1 and g_2 denote the half-widths from resonator-1 and resonator-2, respectively. For first-order, g_{12} is just the sum of the thermal and viscous losses on the cylindrical wall in the center section of resonator-1. We used equation (6) to examine the differences between the measured and calculated half-widths for the virtual resonator.

3. Apparatus and measurements

Figure 3 shows the 80 mm resonator on a support plate that was hung from thin rods. The rods were hung from springs that were attached to the lid of a pressure vessel. The 160 mm resonator (not shown) was hung in the same way from the same lid.

A common manifold supplied argon gas from a single source to both resonators through a tee union. Both resonators were operated at nearly identical temperatures and pressures and at nearly identical frequencies. Furthermore, data were acquired from both resonators at the same time, thereby reducing the time needed for measurements. In hindsight, these advantages may have been offset by an un-modeled coupling between the resonators, as discussed in section 7 below.

The 80 mm long resonator is the same one that we used in a previous measurement of k_B [11]. The 160 mm resonator was constructed to resemble the 80 mm resonator as closely as possible. The cylindrical portions of both resonators were made from the same billet of bearing steel. Both cylinders had nominal inner diameters of 80 mm and wall thicknesses of 40 mm. The cross-section of each cylinder was circular within 0.01 mm. As explained in our previous publication [11], two ends of a practical cylinder cavity are tilted at an angle. According to the request of the laser interferometry and the capability of machining, we designed the machining tolerance for the tilted angle for each cylinder to be within the range $(4.2 \text{ to } 5.8) \times 10^{-6}$ radians, which is equivalent to $0.5 \mu\text{m}$ to $0.7 \mu\text{m}$ across the chosen diameters. The optical length between the end-plates of each resonator was measured using two-color interferometry, as described previously [11]. The fractional uncertainty of the length measurement was 0.28×10^{-6} for the 160 mm resonator and 0.81×10^{-6} for the 80 mm resonator.

The end-plates of each cavity were 15 mm thick and were made from the same block of optical quartz glass. The

end-plate surfaces inside the cavity were coated with a partially reflecting metal film. The clamping rings and bolts holding each end-plate in place were of similar construction. The bolts were machined from the same billet of bearing steel used to fabricate the cylindrical cavities. The bolts were unlubricated and were tightened to the same torque. Nominally identical piezoelectric transducers made from lead zirconium titanate (PZT) were embedded in wells that had been ground into the outside surface of each fused quartz end-plate. The bottom of each well served as a quartz diaphragm transmitting sound into or out of the cavity but preventing the gas in the cavity from mixing with the gas in the pressure vessel outside the cavity. Fill ducts with nominally identical dimensions led from one end of the cylindrical wall of each cavity to a single gas purifier/manifold. Additional details concerning the resonators can be found in our previous publication [11]

As described in section 5.2 of our previous publication [11], each standard capsule platinum resistance thermometer was enclosed in a sealed sleeve to provide the same thermal conditions as the calibration. Then, an enclosed thermometer was placed into each of the wells that had been drilled into opposite ends of the cylindrical wall of each resonator (figure 3). When data were taken, the differences between the average temperatures indicated by each thermometer pair were within ± 0.1 mK; this indicates that each resonator was nearly isothermal. The difference between the average temperatures of the two resonators was no more than ± 0.3 mK. These differences are a measure of the temperature inhomogeneity inside the pressure vessel. The thermometers were calibrated before and after the measurements and they performed as well as the thermometers described previously [11]. The difference between the averages of the initial and final calibrations of each thermometer was less than ± 0.05 mK, which indicates the thermometers were stable during the month-long series of measurements. The triple point of water (TPW) cell that was used for the calibrations was corrected for the isotopic composition of the water. As described previously [11], the TPW cell had been compared with NIM's national reference TPW cells, which, in turn, had been compared with TPW cells of other national metrology institutes.

In this work, we used 'BIP Plus' argon taken from the same container that supplied the argon for cases I and II during our recent measurement of k_B , as described previously [11]. The same reference provides evidence that the average molar mass of this argon was $M = 39.947810(10)$ g mol⁻¹, and we used this value of M to compute k_B for the present data. In a future publication, we will describe extensive, new GC-MS (gas chromatography–mass spectroscopy) measurements and speed-of-sound ratio measurements that have refined the value of M for the argon in this cylinder and reduced its uncertainty. However, the small change in M is not significant for evaluating the virtual resonator concept.

We studied the longitudinal acoustic modes of the argon-filled cavities at 3.8 kHz, 5.8 kHz, and 7.7 kHz. Figure 4 displays a semi-log plot of the acoustic spectrum measured at the detector transducers while both cavities were evacuated. Below 6.1 kHz, both spectra in figure 4 are featureless. Therefore, we did not expect the mechanical resonances either

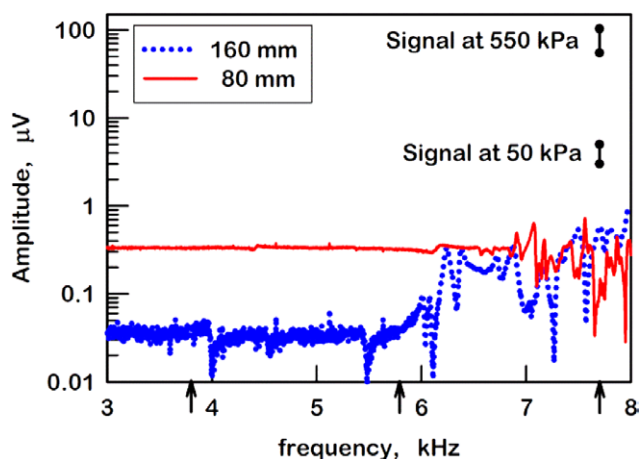


Figure 4. Acoustic spectrum measured while the resonators were evacuated. The arrows indicate the approximate frequencies of the gas modes studied. The range of amplitudes for the gas modes at 50 kPa and 550 kPa at 7.7 kHz are shown for comparison.

of the cylinders or of their supports to strongly perturb the gas resonances. Above 6.1 kHz, the amplitudes of the gas resonances at 550 kPa were $50 \times$ larger than the features in figure 4; however, at 50 kPa, the amplitudes of the gas resonances were only five-times \times larger than the features in figure 4. Therefore, we did not expect these features to cause problems at the higher pressures, but they could cause problems at low pressures. (We note that mechanical resonances related to joints or other small gaps are usually damped when they are filled with gas at high pressure.)

4. Frequency data and uncertainties

Before measuring the resonance frequencies we filled the cavities with argon to either 550 kPa or 500 kPa. As the measurements proceeded, we reduced the pressure in steps of 100 kPa and ended at 50 kPa while maintaining the temperature within 0.6 mK of T_{TPW} . On each pressure step, we measured the frequencies of the longitudinal modes $\ell = 2, 3$, and 4 of the 80 mm resonator and the modes $\ell = 4, 6$, and 8 of the 160 mm resonator repeatedly (4 to 8 times). We repeated the isotherm a total of six times. We reduced the repeated frequency measurements to identical temperatures and pressures and then computed their averages and standard deviations for further processing. Next, we describe how we used the standard deviations of the repeated measurements to objectively weight the sound speed data to fit the pressure dependence. If random noise is dominant, then we expect the standard deviations of the frequencies and half-widths, σ_f and σ_g , to be approximately equal in value and to be power-law functions of the quality factor Q only. The log-log plots in figure 5 show σ_f/f and σ_g/f as a function of Q .

The top panel in figure 5 displays the Q -dependence of the scaled standard deviations of the measured frequencies σ_f/f and measured half-widths σ_g/f for the 3.8 kHz modes of both resonators ($\ell = 2$ mode of the 80 mm resonator and $\ell = 4$ mode of the 160 mm resonator). The Q s are the quality factors of the resonances; at low pressures, they are dominated

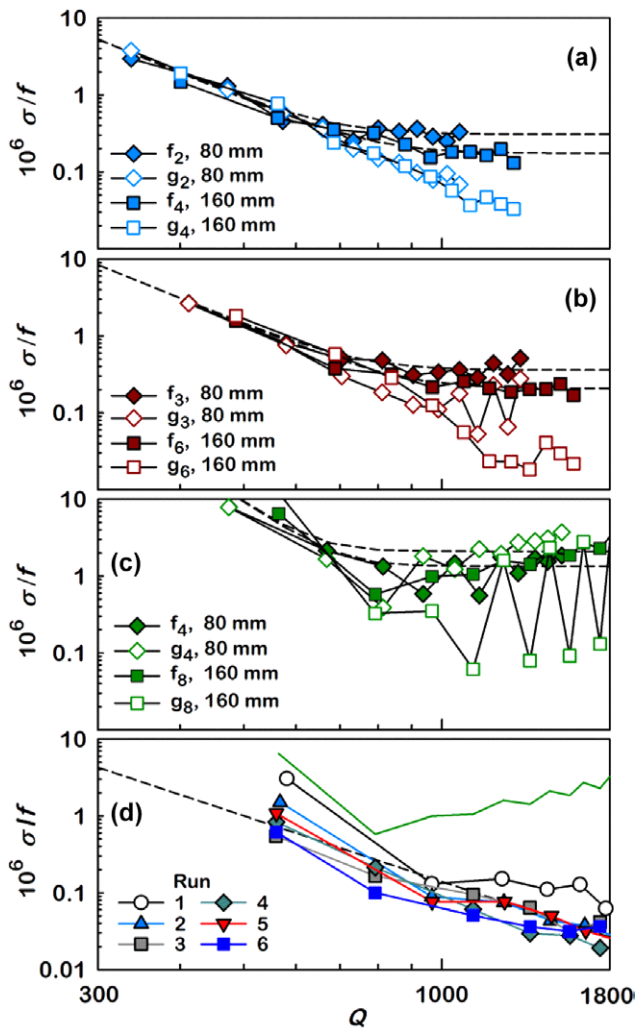


Figure 5. (a)–(c) Plotted points: standard deviation of frequency and half-width measurements over six runs as a function of the quality factor Q of the resonances. During each run, the frequency was measured four to eight times. The smooth dashed curves were used to calculate weights when fitting the frequency measurements to functions of the pressure. (d) Plotted points: standard deviation of the frequency for mode 8 in the 160 mm resonator for individual runs. Solid curve without symbols: standard deviation of the combined data for the six runs from panel (c) shown for comparison.

by boundary losses that vary as $p^{-1/2}$. As expected σ_f/f and σ_g/f are approximately equal at low pressures (corresponding to low Q), reaching a value of approximately 4×10^{-6} at 50 kPa. As the Q s increase, the values of σ_f/f decrease and then level off near $(0.2 \text{ to } 0.3) \times 10^{-6}$. The lower bounds to σ_f/f are determined by small changes in the temperature and/or pressure of the argon. The dashed curves passing through the plotted values of σ_f/f have the functional form: $\sigma_f/f = [a^2 + (bQ^{-c})^2]^{1/2}$. We used $(2c^2\sigma_f/f)N^{-1/2}$, where N is the number of repeated measurements, to determine weights when we fitted functions of the pressure to the measured values of c^2 . The weights ranged from 40 at the lowest pressure to 2×10^4 at the highest pressure. Therefore, the data at 50 kPa had very low relative weight.

For each *separate run*, the values of σ_f/f for the 7.7 kHz modes of both resonators were comparable to those of the

3.8 kHz modes (figure 5(d)). However, the run-to-run variations of f and g at 7.7 kHz were approximately 10-times larger than the values of σ_f/f and σ_g/f at 3.8 kHz. When the run-to-run variations were large, the average frequencies measured during runs starting at 550 kPa differed from those starting at 500 kPa. These differences appear in figure 5(c) as ‘saw-tooth’ patterns at high Q . For the 5.8 kHz modes of both resonators (figure 5(b)), the run-to-run variations of f were approximately twice those indicated by the dashed curves figure 5(a).

5. Fitting $f(T, p, \text{mode})$ surface

Before fitting functions of the pressure to the frequency data, we corrected the measurements to account for the presence of the thermal and viscous boundary layers and the fill duct, and for center-of-mass motion. For each resonator, we used the resonator’s measured length to determine the speed of sound $c_{\text{meas},\ell}$ for the mode ℓ from the corrected frequencies at each state point. In addition, we used equations (4) and (5) to determine the speed of sound using the virtual resonator concept. This procedure generated three sets of sound speed data: one set for the 80 mm resonator, one set for the 160 mm resonator, and one set for the virtual resonator. We correlated the measured speed of sound in each data set with the 8-parameter surface

$$c_{\text{meas},\ell}^2 - A_3 p^3 = A_{0,\ell} + A_{1,\ell} p + A_2 p^2 + A_{-1} p^{-1} \quad (7)$$

by adjusting the coefficients $A_{0,\ell}$, $A_{1,\ell}$, A_2 , and A_{-1} , where the subscript ‘ ℓ ’ identifies the mode-dependent parameter, to optimize χ^2 . Because the maximum pressure was only 550 kPa, we fixed the coefficient A_3 to the value $1.45 \times 10^{-18} \text{ m}^2 \text{ s}^{-2} \text{ Pa}^{-3}$ [4] to avoid over-fitting the data. We weighted the data by N/σ^2 , using values of σ generated by the smooth curves in figure 5. With this weighting, the measurements at 50 kPa had a negligible influence on the parameters k_B , A_1 , and A_2 ; in most cases, A_{-1} was insignificant. Because of the run-to-run variations, the measurements at 7.7 kHz had much less influence on the parameters than those at 3.8 kHz and 5.8 kHz.

The parameters obtained from the surface fits are listed in table 1, and the differences from reference values are displayed in figure 6. The virtual resonator formed by combining data from the (2,0,0) mode of the shorter resonator and the (4,0,0) mode of the longer resonator yielded a value for k_B that is, fractionally, only $(0.2 \pm 1.5) \times 10^{-6}$ larger than the 2010 CODATA-recommended value of k_B , where the estimated uncertainty includes correlations with the other 7 parameters of the surface fit. (All estimated uncertainties are one standard uncertainty corresponding to the 68% confidence level.) The same virtual resonator yielded values of the pressure derivatives of the speed of sound c in argon, $(\partial c^2/\partial p)_T$ and $(\partial^2 c^2/\partial p^2)_T$, that are closer to literature values than the values of k_B , $(\partial c^2/\partial p)_T$, and $(\partial^2 c^2/\partial p^2)_T$ from either cavity, considered separately (figure 6).

Figure 7 displays the differences between the values of c^2 determined using the virtual resonator 3.8 kHz and the values of c^2 from the literature [1, 4]. The results are surprisingly

Table 1. Fitted parameters and derived quantities.

80 mm		160 mm		Virtual		Unit
Parameter	Value	Parameter	Value	Parameter	Value	
$A_{0,2}$	94 755.42(13)	$A_{0,4}$	94 755.76(6)	$A_{0,2,4}$	94 756.09(14)	m^2s^{-2}
$A_{0,3}$	94 755.31(14)	$A_{0,6}$	94 756.72(6)	$A_{0,3,6}$	94 758.12(14)	m^2s^{-2}
$A_{0,4}$	94 755.57(15)	$A_{0,8}$	94 757.14(11)	$A_{0,4,8}$	94 758.82(20)	m^2s^{-2}
$10^4 A_{1,2}$	2.0325(52)	$10^4 A_{1,4}$	2.1402(25)	$10^4 A_{1,2,4}$	2.2481(54)	$\text{m}^2\text{s}^{-2}\text{Pa}^{-1}$
$10^4 A_{1,3}$	2.0613(53)	$10^4 A_{1,6}$	2.1277(25)	$10^4 A_{1,3,6}$	2.1938(54)	$\text{m}^2\text{s}^{-2}\text{Pa}^{-1}$
$10^4 A_{1,4}$	1.9412(55)	$10^4 A_{1,8}$	2.0883(35)	$10^4 A_{1,4,8}$	2.2336(66)	$\text{m}^2\text{s}^{-2}\text{Pa}^{-1}$
$10^{11} A_2$	5.041(60)	$10^{11} A_2$	5.126(29)	$10^{11} A_2$	5.212(60)	$\text{m}^2\text{s}^{-2}\text{Pa}^{-2}$
$10^{-2}A_{-1}$	314(98)	$10^{-2}A_{-1}$	185(46)	$10^{-2}A_{-1}$	-0.91 ± 110	$\text{m}^2\text{s}^{-2}\text{Pa}$
χ^2/ν	2.2	χ^2/ν	1.6	χ^2/ν	0.8	
Derived quantities						
$10^4 \langle A_1 \rangle$	2.012(63)	$10^4 \langle A_1 \rangle$	2.119(27)	$10^4 \langle A_1 \rangle$	2.225(28)	$\text{m}^2\text{s}^{-2}\text{Pa}^{-1}$
$\langle A_0 \rangle$	94 755.43(13)	$\langle A_0 \rangle$	94 756.54(71)	$\langle A_0 \rangle$	94 757.68(142)	m^2s^{-2}
$10^{23} \langle k_B \rangle$	1.380 639 5(18)	$10^{23} \langle k_B \rangle$	1.380 655 7(103)	$10^{23} \langle k_B \rangle$	1.380 672 3(207)	JK^{-2}

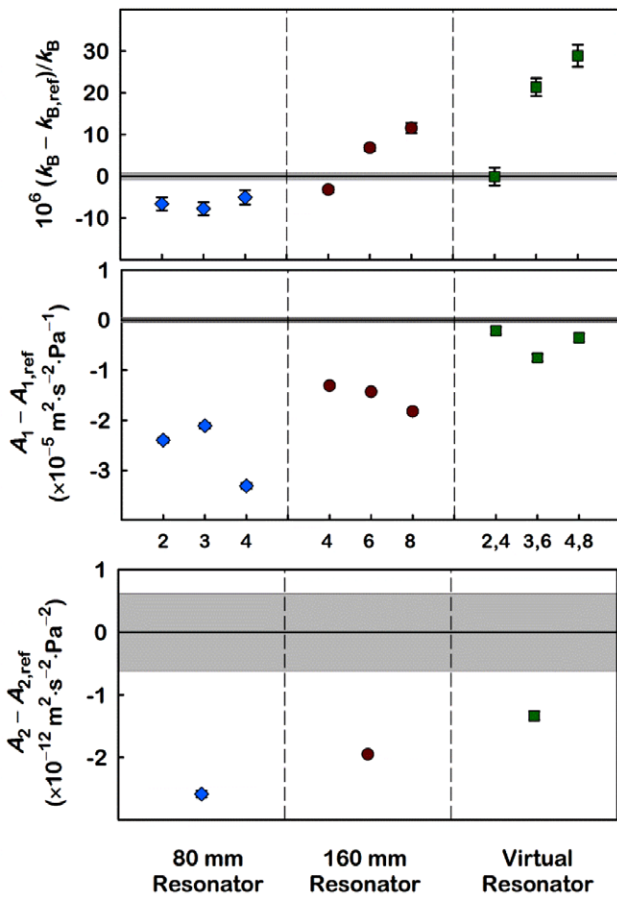


Figure 6. Results from surface fits of the data for each resonator separately and from the virtual-resonator analysis. The uncertainty bars on the plotted points include only type-A uncertainties from fitting. The horizontal axis labels ‘2’, ‘3’, ... indicate the (2,0,0), (3,0,0), ... modes. Top panel: baseline for k_B comes from CODATA-2010 [1]. The baselines for the middle panel [$A_1 \equiv (\partial c^2/\partial p)_T$] and for the lower panel [$A_2 \equiv (\partial c^2/\partial p^2)_T$] come from another publication [4]. The gray widths of the baselines represent their uncertainties as given elsewhere [1,4].

good. In contrast, the values of k_B , A_1 , and A_2 (hence the values of c^2) obtained from the 5.8 kHz and 7.7 kHz virtual resonators are much worse (figure 6).

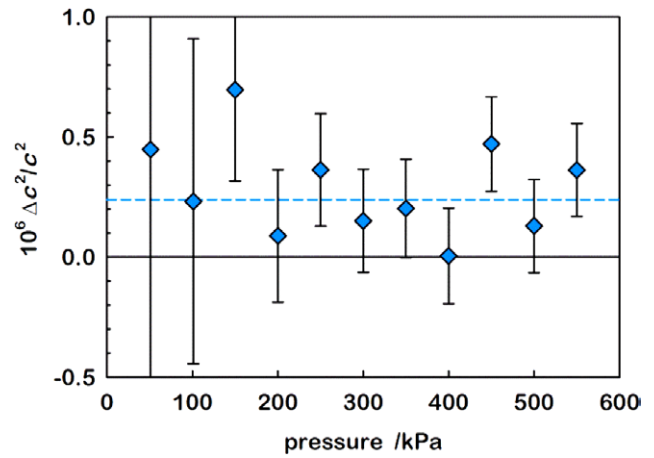


Figure 7. Deviations of c^2 from the CODATA value of A_0 for the virtual resonator at 3.8 kHz resulting from the surface fit corresponding to the right-most panels in figure 6. The dashed line is the baseline for the mode from the surface fit. The error bars are $(2\sigma/f)/N^{1/2}$ from the average of the repeated measurements.

6. Half-width data

Figure 8 shows the differences $\Delta g/f \equiv (g_{\text{meas}} - g_{\text{calc}})/f$ between the measured and calculated values of g/f for the individual modes in the 80 mm and 160 mm resonators and for the virtual resonator modes as a function of pressure. Our model for acoustic resonators predicts g/f based on known energy loss mechanisms, including the contribution to g due to the presence of the fill duct and, for second-order, thermal conduction and viscous drag effects that occur in the volume of gas and near the wall of the resonator [16]. For the virtual resonator, we plot the difference between equation (6) evaluated with the measured half-widths and equation (6) evaluated with the calculated half-widths. The bottom panel of figure 8 shows that $\Delta g/f$ for the 3.8 kHz virtual resonator (labeled 2,4) is less than $\Delta g/f$ for mode 2 in the 80 mm resonator and mode 4 in the 160 mm resonator at all pressures. In contrast, $\Delta g/f$ for the 5.8 kHz virtual resonator (labeled 3,6) is lower than $\Delta g/f$ for modes 3 and 6 in the individual resonators at high pressures but not at low pressures. The values of $\Delta g/f$ for the virtual

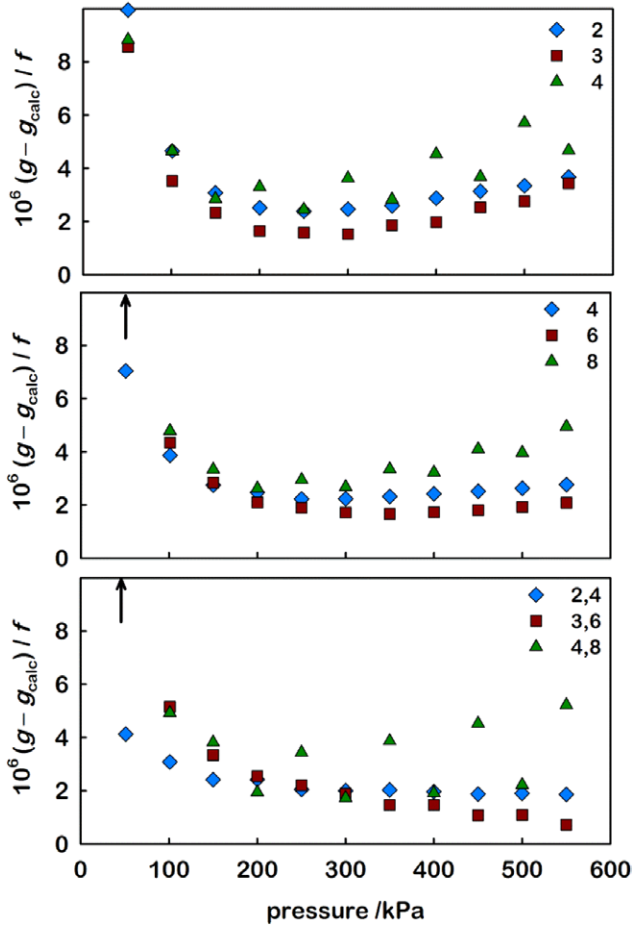


Figure 8. Excess half-widths for modes 2, 3, and 4 in the 80 mm resonator (top), modes 4, 6, and 8 in the 160 mm resonator (middle), and the virtual resonator from equation (6) (bottom).

resonator at 7.7 kHz (labeled 4,8) and for modes 4 and 8 in the individual resonators alternate between high and low values that were obtained from different runs.

7. Discussion of puzzling results

7.1. Bad values of c_0^2 at 5.8 kHz and 7.7 kHz

Figure 9 displays the deviations of the speed of sound determined using the 7.7 kHz virtual resonator (with no adjusted parameters) from literature values. At low pressures, the deviation curves converge to the run-independent value $(c_0^2/c_{ref}^2 - 1) \approx 25 \times 10^{-6}$. When inspecting the figure, it is useful to ignore the lightly weighted, noisy data at 50 kPa. This large discrepancy (25×10^{-6}) cannot be attributed to impurities in the argon, nor to an unexpected change in the length of one of the resonators because the 3.8 kHz virtual resonator operating at the same time with the same gas yielded the expected values of k_B and c_0^2 in the low-pressure limit: $(k_B/k_{B,ref} - 1) = (0.2 \pm 1.5) \times 10^{-6}$. Furthermore, the discrepancy of 25×10^{-6} cannot be attributed to a perturbation of the acoustic (gas) oscillations by the resonators' compliance. Such perturbations generate frequency-dependent deviations that are proportional to $(\rho c^2)_{gas}$ and vanish in the limit of zero pressure [12]. (Here, ρ is the mass density of the gas.)

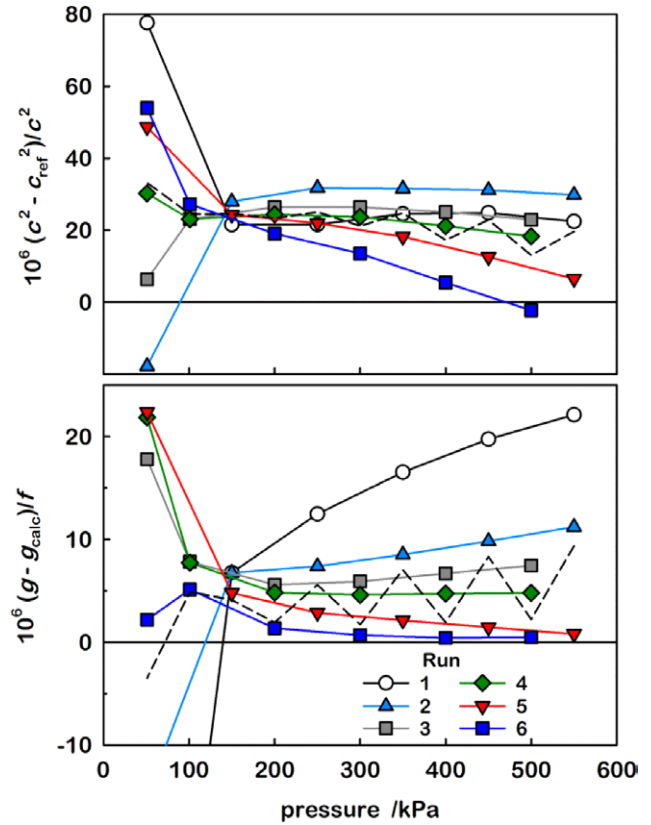


Figure 9. Run-dependent performance of the 7.7 kHz virtual resonator; no adjusted parameters. (top) Deviations of c^2 determined using equation (4) from reference values [4]. (bottom) $\Delta g/f$ determined using equation (6). In both plots, the dashed lines show the result of averaging over all six runs.

7.2. Excess half-widths at low pressures

The top and middle panels of figure 8 show that $\Delta g/f$ increases as the pressure is reduced below 200 kPa for all the modes that we studied in both resonators. We do not have an explanation for this behavior. We expect that the energy loss from un-modeled interactions between the acoustic waves in the gas and the solid structures diminishes as $(\rho c^2)_{gas} \propto p \rightarrow 0$. The value of $\Delta g/f$ for the 3.8 kHz virtual resonator at the lowest pressure is approximately half of $\Delta g/f$ for the individual resonators at the same pressure, which suggests that some of the extra energy loss at this frequency in both resonators may have a common origin. However, $\Delta g/f$ for the 5.8 kHz and 7.7 kHz virtual resonators is larger than $\Delta g/f$ for the individual resonators at low pressure, which suggests there is a significant difference in the origin of the energy loss in the individual resonators at low pressure. Furthermore, the bottom panel of figure 9 shows that the excess half-widths (or unexplained energy losses) for the 7.7 kHz virtual resonator are run-dependent (with no adjusted parameters) and converge to a non-zero value at zero pressure.

7.3. Run-dependent values of A_1 and A_2

The top panel of figure 9 reveals that both A_1 (the slope of the deviations) and A_2 (the curvature of the deviations) differ from

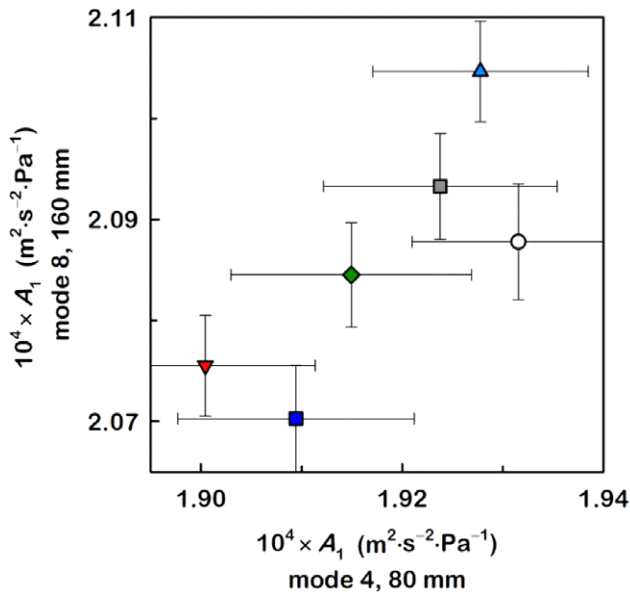


Figure 10. Correlation of the run-dependent values of A_1 measured at 7.7 kHz with the 80 mm resonator and the 160 mm resonator.

their expected values in a run-dependent manner. Because we did not detect a similar run dependence in the data from the 3.8 kHz virtual resonator, the run dependences of A_1 and A_2 cannot be attributed to changes in composition of the gas.

The perturbation of the acoustic oscillations by the resonators' compliance predicts that A_1 is frequency-dependent (or, equivalently, mode-dependent). Pitre *et al* [5] argued that A_2 also would be mode-dependent if an acoustic mode happened to be close to a resonance of the shell. Figure 4, which shows numerous shell resonances above 6.1 kHz, supports that argument. To account for run dependence, however, we would have to argue that the process of emptying and refilling the pressure vessel shifted resonance frequency of the shell relative to the resonance frequencies of the gas. Even if run-dependent gas-shell interactions caused the anomalous pressure dependence at 7.7 kHz, we remind the reader that gas-shell interactions do not explain the erroneous values of c_0^2 discussed in section 7.1.

However, figure 10 shows that the run-dependent values of A_1 measured at 7.7 kHz with the 80 mm resonator are highly correlated with the values measured with the 160 mm resonator. (The correlation coefficient is 0.8.) This suggests that a run-dependent phenomenon is coupled to both resonators.

Figure 11 compares the half-widths of the (8,0,0) mode of the 160 mm resonator and the (4,0,0) mode of the 80 mm resonator to the difference between the frequencies of these two modes: $f_{8,160\text{mm}} - f_{4,80\text{mm}}$. The frequency difference is 1/5 of the combined half-widths at 550 kPa and decreases to 1/9 of the combined half-widths at 100 kPa. Thus, the two modes overlap. If, for example, the acoustic detector on the 80 mm resonator had some weak response to acoustic oscillations within the 160 mm resonator, then this would have generated a small distortion of the resonance line shape that might not have been detected. Such a coupling could affect the fitted resonance frequencies and half-widths in unpredictable ways.

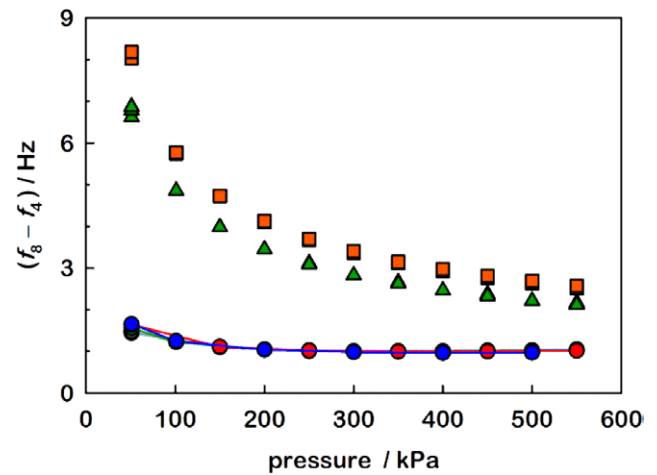


Figure 11. Half-widths of the 7.7 kHz modes of the 80 mm (squares) and 160 mm (triangles) resonators are much larger than the frequency differences between these two modes (circles).

8. Conclusion

We showed that the virtual resonator at 3.8 kHz, formed from the (2,0,0) mode of the 80 mm resonator and the (4,0,0) mode of the 160 mm resonator, gave a value for k_B that was only $(0.2 \pm 1.5) \times 10^{-6}$ larger than the 2010 CODATA-recommended value. Furthermore, the values for A_1 and A_2 from the virtual resonator were nearly consistent with literature values when the values from the individual resonators were not. The results at 3.8 kHz demonstrate success of the virtual resonator at reducing the systematic errors that are present in the individual resonators.

In contrast, the virtual resonator at 5.8 kHz, formed from the (3,0,0) mode of the 80 mm resonator and the (6,0,0) mode of the 160 mm resonator, and the virtual resonator at 7.7 kHz, formed from the (4,0,0) mode of the 80 mm resonator and the (8,0,0) mode of the 160 mm resonator, gave surprisingly poor values of k_B . We show that the data at 5.8 kHz and 7.7 kHz exhibited pathological behaviors that were not removed by the virtual resonator analysis and were not present in the data at 3.8 kHz.

We speculate that the two resonators were weakly coupled to each other, either electrically or mechanically, and that the coupling was lossy. Therefore, their resonance frequencies were determined, in part, by the coupling, much like the textbook problem of coupled pendula [21].^{3,4} This hypothetical lossy coupling had to be present, even when the pressure in the common pressure vessel was quite low, to explain the erroneous values of c_0^2 that we obtained at 5.8 kHz and 7.7 kHz and to explain the large excess half-widths. Such a coupling, if it exists, may be eliminated either by measuring the frequencies and half-widths on the isotherm with only one resonator in the pressure vessel at a time or by using resonators whose lengths differ from a factor of two by enough that the frequencies do not overlap. We plan to pursue one or both of these strategies.

³ See, for example [21].

⁴ For a more advanced discussion of coupled oscillators, see [21].

Acknowledgments

This work was supported by the National Natural Science Foundation of China (51476153, 51276175, and 51106143).

References

- [1] Mohr P J, Taylor B N and Newell D B 2012 *Rev. Mod. Phys.* **84** 1527–605
- [2] Quinn T J, Colclough A R and Chandler T R D 1976 *Proc. R. Soc. Lond. A* **283** 367–420
- [3] Colclough A R, Quinn T J and Chandler T R D 1979 *Proc. R. Soc. Lond. A* **368** 125–39
- [4] Moldover M R, Trusler J P M, Edwards T J, Mehl J B and Davis R S 1988 *J. Res. Natl Bur. Stand.* **93** 85–144
- [5] Pitre L, Sparasci F, Truong D, Guillou A, Riseigari L and Himbert M E 2011 *Int. J. Thermophys.* **32** 1825–86
- [6] Pitre L, Guianvarc'h C, Sparasci F, Guillou A, Truong D, Hermier Y and Himbert M E 2009 *C. R. Phys.* **10** 835–48
- [7] de Podesta M, Underwood R, Sutton G, Morantz P, Harris P, Mark D F, Stuart F M, Vargha G and Machin G 2013 *Metrologia* **50** 354–76
- [8] Gavioso R M, Benedetto G, Albo P A G, Ripa D M, Merlone A, Guianvarc'h C, Moro F and Cuccaro R 2010 *Metrologia* **47** 387–409
- [9] Sutton G, Underwood R, Pitre L, Podesta M D and Valkiers S 2010 *Int. J. Thermophys.* **31** 1310–46
- [10] Zhang J T, Lin H, Feng X J, Sun J P, Gillis K A, Moldover M R and Duan Y Y 2011 *Int. J. Thermophys.* **32** 1297–331
- [11] Lin H, Feng X J, Gillis K A, Moldover M R, Zhang J T, Sun J P and Duan Y Y 2013 *Metrologia* **50** 417–32
- [12] Moldover M R, Gavioso R M, Mehl J B, Pitre L, de Podesta M and Zhang J T 2014 *Metrologia* **51** R1–9
- [13] Gillis K A, Lin H and Moldover M R 2009 *J. Res. Natl Inst. Stand. Technol.* **114** 263–85
- [14] Lin H, Gillis K A and Zhang J T 2010 *Int. J. Thermophys.* **31** 1234–47
- [15] Zhang J T, Lin H, Sun J P, Feng X J, Gillis K A and Moldover M R 2010 *Int. J. Thermophys.* **31** 1273–93
- [16] Gillis K A 2012 *Metrologia* **49** L21–4
- [17] Zhang J T, Lin H and Feng X J 2012 *9th Int. Temperature Symp (Los Angeles, CA, 19–23 March 2012)*
- [18] Moldover M R 2009 *C. R. Phys.* **10** 815–27
- [19] Rayner G H 1972 *IEEE Trans. Instrum. Meas.* **IM21** 361–5
- [20] Gillis K A 1994 *Int. J. Thermophys.* **15** 821–47
- [21] Becker R A 1954 *Introduction to Theoretical Mechanics* (New York: McGraw-Hill) chapter 14
Morse P M and Ingard K U 1986 *Theoretical Acoustics* (Princeton: Princeton University Press) chapter 3 and section 10.4.